Mathematical Modeling of Impacts of Patient Differences on COVID-19 Lung Fibrosis Outcomes

Mohammad Aminul Islam[a], Ashlee N. Ford Versypt[a,b,c,d,*]

[a] *Department of Chemical and Biological Engineering, University at Buffalo, The State University of New York, Buffalo, NY, 14260, USA*
[b] *Department of Biomedical Engineering, University at Buffalo, The State University of New York, Buffalo, NY, 14260, USA*
[c] *Institute for Artificial Intelligence and Data Science, University at Buffalo, The State University of New York, Buffalo, NY, 14260, USA*
[d] *Witebsky Center for Microbial Pathogenesis and Immunology, University at Buffalo, The State University of New York, Buffalo, NY, 14203, USA*

Abstract

Patient-specific premorbidity, age, and sex are significant heterogeneous factors that influence the severe manifestation of lung diseases, including COVID-19 fibrosis. The renin-angiotensin system (RAS) plays a prominent role in regulating effects of these factors. Recent evidence suggests that patient-specific alteration of RAS homeostasis with premorbidity and the expression level of angiotensin converting enzyme 2 (ACE2), depending on age and sex, is correlated with lung fibrosis. However, conflicting evidence suggests decreases, increases, or no changes in RAS after SARS-CoV-2 infection. In addition, detailed mechanisms connecting the patient-specific conditions before infection to infection-induced fibrosis are still unknown. Here, a mathematical model is developed to quantify the systemic contribution of heterogeneous factors of RAS in the progression of lung fibrosis. Three submodels are connected—a RAS model, an agent-based COVID-19 in-host immune response model, and a fibrosis model—to investigate the effects of patient-group-specific factors in the systemic alteration of RAS and collagen deposition in the lung. The model results indicate cell death due to inflammatory response as a major contributor to the reduction of ACE and ACE2, whereas there are no significant changes in ACE2 dynamics due to viral-bound internalization of ACE2. Reduction of ACE reduces the home-

*Corresponding author email address: ashleefv@buffalo.edu

ostasis of RAS including angiotensin II (ANGII), while the decrease in ACE2 increases ANGII and results in severe lung injury and fibrosis. The model explains possible mechanisms for conflicting evidence of RAS alterations in previously published studies. Also, the results show that ACE2 variations with age and sex significantly alter RAS peptides and lead to fibrosis with around 20% additional collagen deposition from systemic RAS with slight variations depending on age and sex. This model may find further applications in patient-specific calibrations of tissue models for acute and chronic lung diseases to develop personalized treatments.

Keywords: SARS-CoV-2, renin-angiotensin system, TGF-β, pulmonary fibrosis

---

1. Introduction

The renin-angiotensin system (RAS) has gained significant attention as alterations in RAS peptides and enzymes directly correlate with patient-specific premorbidity, age, and sex differences in response to COVID-19 lung diseases [1–4]. RAS is important in maintaining physiological processes, including blood pressure and vascular permeability [1]. The cascade of local and systemic regulatory processes of RAS begins with renin from the kidney and angiotensinogen (AGT) from the liver, which enter into the systemic process through blood and migrate to the lung. The activity of renin on AGT causes its conversion to angiotensin I (ANGI). ANGI uses the angiotensin converting enzyme (ACE) from the cell surface of lung tissue to convert to angiotensin II (ANGII). ANGII binds with angiotensin converting enzyme 2 (ACE2) from the cell surface to form the ACE2•ANGII complex, which converts to angiotensin 1–7 (ANG1–7). ANGII also binds with angiotensin type 1 receptor (AT1R) and forms the ANGII•AT1R complex, which regulates the feedback signaling to the systemic renin production rate. In the subsequent reactions, ANGII binds with angiotensin type 2 receptor (AT2R) and forms the ANGII•AT2R complex, ANGII converts to angiotensin IV (ANGIV) by enzymatic reaction, and ANG1–7 binds with MAS receptor to form the MAS•ANG1–7 complex. The expressions of ACE2 [4] and homeostasis values of RAS peptides [5] are patient-dependent.

Kutz et al. [1] observed reductions in all RAS peptides and renin activity without significant differences in ACE and ACE2 activity in the serum of COVID-19 patients compared with matched controls. Contrarily, N. Liu et

al. [2] reported increased ANGII in critically ill SARS-CoV-2 positive patients compared to non-critically ill SARS-CoV-2 positive patients. Y. Liu et al. [6] observed increased plasma ANGII levels in SARS-CoV-2-infected patients compared to healthy individuals. The up-regulation in ACE2 expression has also been observed in COVID-19 patients [7]. Contrary to all, Kintscher et al. [8] did not observe any significant differences in plasma RAS peptides and ACE2 activity between control and COVID-19 patients. To explain the conflicting data on RAS peptide alteration, Kutz et al. [1] highlighted the differences between their study and that of N. Liu et al. [2], particularly the selection of the baseline patient groups. The baseline patient group in Kutz et al. [1] was SARS-CoV-2-negative, whereas Liu et al. [2] selected SARS-CoV-2-positive patients with normal ANGII range. In addition to these contradictions and limitations of scarce patient data, detailed mechanisms suitable for explaining the conflicting observations in different patient groups still need to be determined.

Patient-specific premorbidity, age, and sex differences can account for the variations in responses between patient groups. Pendergrass et al. [9] observed variations in RAS with sex differences for hypertensive rats. Xudong et al. [10] reported dramatically reduced ACE2 expression with aging and higher ACE2 content in old female rats than in males. In a recent mathematical study, Bastolla [11] showed a direct correlation between the severity of COVID-19 fatality depending on age and sex across three countries and experimental data for the expression of ACE2 from Xudong et al. [10]. Miesbach [12] reported that male patients were more affected by severe manifestations than female patients and depended on the activation of RAS and pathological roles of ANGII.

Downregulation of ACE2 inhibits the protective activity of downstream RAS peptides, resulting in inflammation and fibrosis [13, 14]. RAS regulates the fibrosis process by directly and indirectly activating and inhibiting latent TGF-β [15]. ANGII•AT1R complex in RAS activates latent TGF-β directly or via Smad and ERK/p38/MAPK signaling pathways, whereas ANGII•AT2R complex inhibits TGF-β production. Via *in vitro* experiments, ANGII•AT1R was reported to induce procollagen synthesis from human fetal lung fibroblasts directly through mitogenesis and indirectly through TGF-β [16]. ANGII-induced TGF-β production was also observed in vascular smooth muscle cells [17] and glomerular mesangial cells [18]. In our earlier mathematical modeling work [19], we also identified TGF-β as a critical contributor to COVID-19 fibrosis. TGF-β activates and recruits macrophages

and fibroblasts, and fibroblasts are responsible for excess collagen deposition and fibrosis [19–21].

Bleomycin-mouse models are widely used to evaluate the effect of RAS peptides and enzymes in lung fibrosis [22]. Li et al. [23] observed increased ANGII and collagen for ACE2 knockout mice in bleomycin-induced lung fibrosis models. Rey et al. [24] also ran similar experiments for ACE2 knockout male and female mice and observed increased collagen in both males and females with significantly increased collagen in males compared to females [24]; they also highlighted that a higher AT2R/AT1R ratio in female mice could be a possible explanation for the sex differences in collagen deposition. The bleomycin-induced lung fibrosis mouse model of Kuba et al. [25] showed increased ANGII in the presence of SARS-CoV spike proteins. Another study from the same lab reported that ACE2 knockout mice also increased ANGII [26]. The mouse model of Wang et al. [27] showed exogenous ACE2 attenuates bleomycin-induced lung injury by attenuating TGF-β production and collagen deposition.

Multiple computational and mathematical models have been developed to integrate and quantify the effect of premorbidity, age, and sex differences in RAS and RAS-mediated fibrosis. Leete et al. [28] developed a mathematical model to investigate the effect of sex differences in RAS, and they identified ANGII•AT1R feedback mechanism as a significant modulator of sex differences. Pucci et al. [29] developed a mathematical model to investigate the pathogenic mechanisms of SARS-CoV-2 and RAS and applied their model for *in silico* testing of potential modulators to restore functionality. Sadria and Layton [30] expanded a RAS model with membrane-bound ACE2, shedding of ACE2, and internalized ACE2; connected that to a damage response model; and used the model to investigate the effects of drugs targeting ACE and AT1R. The mathematical modeling framework of Voutouri et al. [31] connected SARS-CoV-2 infection, RAS, innate and adaptive immune cells, and coagulation cascade to investigate the heterogeneity in treatment response and clinical outcome as a function of patient comorbidities, age, and immune response; the model predicted increases in ANGII in severe COVID-19 patients. Barbiero and Lió [32] developed a computational patient model integrating cardiovascular, RAS, and diabetic processes; and they analyzed the effects of age, diabetes, and renal impairment during SARS-CoV-2 infection in a functional context. Our lab has also previously developed mathematical models of RAS for normal and impaired renal functions [33] and glucose dependency of RAS in diabetic kidney disease [34, 35].

Here, we developed a mathematical model that contributes to understanding patient-specific premorbidity, age, and sex differences in COVID-19 lung fibrosis. We connected a RAS model to our earlier agent-based model (ABM) framework for COVID-19 immune response in the lung [36] and our fibrosis model [19] to investigate and quantify the local and systemic effects of the heterogeneous factors of RAS in the progression of fibrosis due to SARS-CoV-2 infection.

2. Methodology

2.1. COVID-19 RAS fibrosis model

The COVID-19 RAS fibrosis model (Fig. 1) consists of three submodels: a RAS model to account for patient-specific local and systemic changes of RAS peptides and enzymes, an ABM COVID-19 in-host immune response model to quantify tissue scale dynamics of ACE2 receptor trafficking and inflammatory immune response due to SARS-CoV-2 infection, and a fibrosis model to quantify the effects of immune modulation by dysregulated RAS peptides and systemic contributions to lung fibrosis. We refer to the COVID-19 RAS fibrosis model as the "overall model". Each of the submodels is detailed in turn.

2.1.1. RAS model

The rate of change of renin is

$$\frac{d[R]}{dt} = \beta - \frac{\ln 2}{h_R}[R] \tag{1}$$

$$\beta = \begin{cases} \beta_0, & \text{if no feedback} \\ \beta_0 + \left(\left(\frac{[ANGII \cdot AT1R_0]}{[ANGII \cdot AT1R]} \right)^{\delta} - 1 \right), & \text{else if } [ANGII \cdot AT1R] \geq 1 \frac{fmol}{mL} \\ \beta_0 + \left([ANGII \cdot AT1R_0]^{\delta} - 1 \right), & \text{otherwise} \end{cases} \tag{2}$$

where $[R]$ is renin concentration, β is the production rate, and h_R is the half-life of renin. The term β has two contributions: a constant source of renin from the kidney, β_0, and feedback of ANGII•AT1R to the production of renin, given by (2). The strength of the feedback signaling is defined by a dimensionless number, δ.

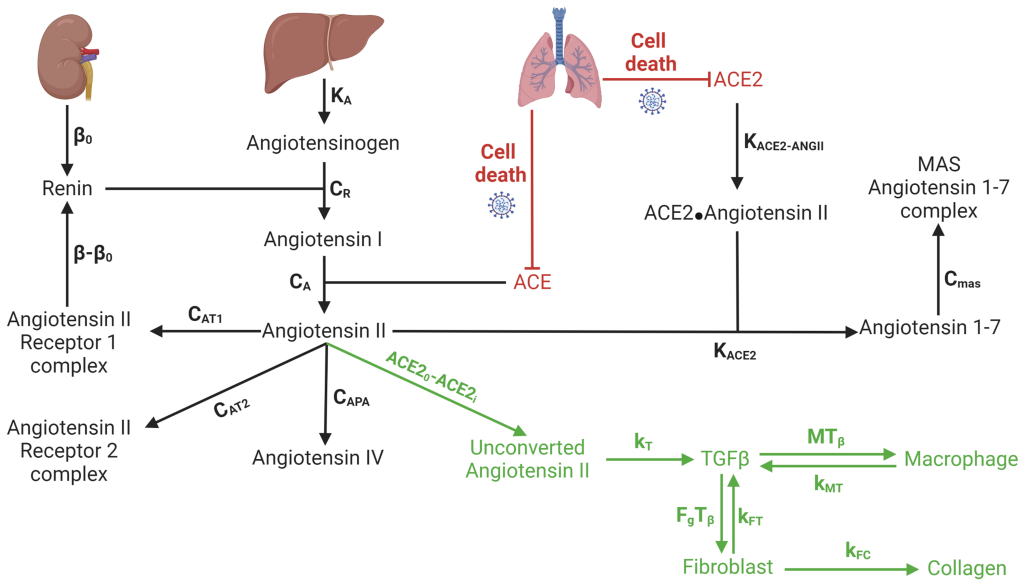

Figure 1: Schematic diagram of COVID-19 RAS Fibrosis model. RAS maintains a patient-specific homeostasis before SARS-CoV-2 infection. During infection, the death of epithelial cells downregulates both ACE and ACE2, which increases unconverted ANGII. Unconverted ANGII induces TGF-β production and activates the fibrosis cascade.

The rate of change of AGT is

$$\frac{d[AGT]}{dt} = k_A - c_R[R] - \frac{\ln 2}{h_A}[AGT] \tag{3}$$

where $[AGT]$ is concentration of AGT, k_A is a constant source of AGT from the liver, c_R relates renin concentration to its activity on AGT, and h_A is the half-life of AGT. Here, we assume a constant renin activity (constant c_R). This simplified model does not account for the variations in the renin activity due to the changes in plasma renin activity (PRA) [28, 31, 33].

The rate of change of ANGI is

$$\frac{d[ANGI]}{dt} = c_R[R] - c_A[ANGI]ACE(t) - \frac{\ln 2}{h_{A1}}[ANGI] \tag{4}$$

where $[ANGI]$ is concentration of ANGI, c_A is the rate constant for ACE catalyzed conversion of ANGI to ANGII, $ACE(t)$ is the ACE receptor profile

determined from the other submodels and described in Section 2.1.3, and h_{A1} is the half-life of ANGI.

The rate of change of ANGII is

$$\frac{d[ANGII]}{dt} = c_A[ANGI]ACE(t) - c_{APA}[ANGII] - c_{AT1}[ANGII] - c_{AT2}[ANGII] - k_{ACE2\cdot ANGII}[ANGII]ACE2(t) - \frac{\ln 2}{h_{A2}}[ANGII] \tag{5}$$

where $[ANGII]$ is concentration of ANGII, c_{APA} is the rate constant for APA catalyzed conversion of ANGII to ANGIV, c_{AT1} and c_{AT12} are the binding rate constants for formation of ANGII•AT1R and ANGII•AT2R, respectively, $k_{ACE2\cdot ANGII}$ is the binding rate constant for formation of ACE2•ANGII, $ACE2(t)$ is the ACE2 receptor profile determined from the other submodels and described in Section 2.1.3, and h_{A2} is the half-life of ANGII.

The rates of change of ACE2•ANGII and ANG1–7 are

$$\frac{d[ACE2 \cdot ANGII]}{dt} = k_{ACE2\cdot ANGII}[ANGII]ACE2(t) - k_{ACE2}[ACE2\cdot ANGII] \tag{6}$$

and

$$\frac{d[ANG1\text{–}7]}{dt} = k_{ACE2}[ACE2\cdot ANGII] - c_{mas}[ANG1\text{–}7] - \frac{\ln 2}{h_{A17}}[ANG1\text{–}7] \tag{7}$$

where $[ACE2 \cdot ANGII]$ and $[ANG1\text{–}7]$ are concentrations of ACE2•ANGII and ANG1–7, respectively, k_{ACE2} is the rate constant for the conversion rate of ACE2•ANGII to ANG1–7, c_{mas} is the binding rate constant for the formation of MAS•ANG1–7, and h_{A17} is the half-life of ANG1–7.

The rate of change of ANGIV is

$$\frac{d[ANGIV]}{dt} = c_{APA}[ANGII] - \frac{\ln 2}{h_{A4}}[ANGIV] \tag{8}$$

where $[ANGIV]$ is concentration of ANGIV and h_{A4} is the half-life of ANGIV.

ANGII binds with AT1R and AT2R receptors, and ANG1–7 binds with MAS receptors. The rates of change of these complexes are

$$\frac{d[ANGII \cdot AT1R]}{dt} = c_{AT1}[ANGII] - \frac{\ln 2}{h_{AT1}}[ANGII \cdot AT1R], \tag{9}$$

$$\frac{d[ANGII \cdot AT2R]}{dt} = c_{AT2}[ANGII] - \frac{\ln 2}{h_{AT2}}[ANGII \cdot AT2R], \tag{10}$$

and

$$\frac{d[MAS \cdot ANG1\text{–}7]}{dt} = c_{mas}[ANG1\text{–}7] - \frac{\ln 2}{h_{mas}}[MAS \cdot ANG1\text{–}7] \tag{11}$$

where $[ANGII \cdot AT1R]$, $[ANGII \cdot AT2R]$, and $[MAS \cdot ANG1\text{–}7]$ are concentrations and h_{AT1}, h_{AT2}, and h_{mas} are the half lives of ANGII•AT1R, ANGII•AT2R, and MAS•ANG1–7, respectively.

Table 1: List of fixed parameters for the overall model

Symbol	Definition	Value	Unit	Source
c_R	Renin activity on AGT	2×10^1	min^{-1}	[29]
h_R	Half-life of renin	1.2×10^1	min	[29, 37]
h_A	Half-life of angiotensinogen	6×10^2	min	[29, 37]
h_{A1}	Half-life of angiotensin I	5×10^{-1}	min	[29, 37]
h_{A2}	Half-life of angiotensin II	5×10^{-1}	min	[29, 37]
h_{A17}	Half-life of angiotensin 1–7	5×10^{-1}	min	[29, 37]
h_{A4}	Half-life of angiotensin IV	5×10^{-1}	min	estimated
h_{AT1}	Half-life of angiotensin II & receptor 1 complex	1.2×10^1	min	[29, 37]
h_{AT2}	Half-life of angiotensin II & receptor 2 complex	1.2×10^1	min	[29, 37]
h_{mas}	Half-life of angiotensin 1–7 & MAS complex	1.20×10^1	min	[29]
δ	Strength of feedback to Renin	8×10^{-1} $[0, 1]$	Unitless	[28, 29]
r_b	Binding rate of virus to ACE2	1×10^{-3}	min^{-1}	[36]
V_c	Volume of epithelial cell	2.494×10^3	μm^3	[36]
DS	TGF-β activation rate from a damaged site	2×10^{-9}	ng min^{-1}	estimated in [19]
MS	TGF-β secretion rate from an M2 macrophage	2×10^{-9}	ng min^{-1}	estimated in [19]
k_T	ANGII-induced TGF-β production rate	7.0×10^{-4}	ng min^{-1} mL fmol^{-1}	estimated
k_{MT}	Macrophage TGF-β production rate	4.86×10^{-5}	min^{-1}	[20, 21]
k_{FT}	Fibroblast TGF-β production rate	2.78×10^{-6}	min^{-1}	[20, 21]
d_T	TGF-β degradation rate	1.04×10^{-2}	min^{-1}	[20]
d_M	Macrophage apoptosis rate	4.17×10^{-4}	min^{-1}	[20, 21]
d_F	Fibroblast apoptosis rate	8.30×10^{-5}	min^{-1}	[20, 21]
k_{FC}	Fibroblast collagen production rate	2.52×10^{-7}	μg min^{-1}	estimated from Ref [38]
$V_{T\beta}$	Rate parameter for TGF-β-dependent collagen deposition	9.42×10^{-1}	Unitless	estimated from Ref [39, 40] data in [19]
$k_{T\beta}$	Saturation parameter for TGF-β-dependent collagen deposition	1.74×10^{-1}	Unitless	estimated from Ref [39, 40] data in [19]
$M(T_\beta)$	TGF-β-dependent macrophage recruitment rate	interpolated	cell min^{-1}	[41]
$F_g(T_\beta)$	TGF-β-dependent fibroblast recruitment rate	interpolated	cell min^{-1}	[41]

The parameters $[R_0]$, β, k_A, c_A, $k_{ACE2 \cdot ANGII}$, k_{ACE2}, c_{APA}, c_{AT1}, c_{AT2}, and $[MAS \cdot ANG1\text{–}7_0]$ in (1)–(11) are patient-specific and require homeostasis values of RAS in calibration. A list of fixed parameters for the overall model are available in Table 1, and mean homeostasis RAS peptide concentrations for normotensive and hypertensive patients are listed in Table 2. We further calibrate the RAS model with the initial number of ACE2 receptors of virtual lung tissue in COVID-19 fibrosis model. We calculate the patient-specific parameters for normotensive and hypertensive patients using the homeostasis values of RAS peptides and the initial number of ACE and ACE2 receptors

Table 2: Homeostasis concentrations of species and parameter values in RAS network for uninfected normotensive and hypertensive patients

Symbol	Definition	Hypertensive	Normotensive	Unit	Source
$[AGT_0]$	angiotensinogen	6×10^5	6×10^5	fmol mL^{-1}	[29, 42]
$[ANGI_0]$	angiotensin I	110	70	fmol mL^{-1}	[9, 29, 43]
$[ANGII_0]$	angiotensin II	156	28	fmol mL^{-1}	[9, 29, 43]
$ANG1\text{–}7_0$	angiotensin 1–7	92	36	fmol mL^{-1}	[9, 29, 43, 44]
$ACE2_0$	angiotensin converting enzyme 2	200–2000	200–2000	cell^{-1}	COVID-19 fibrosis model
$[ACE2 \cdot ANGII_0]$	angiotensin II & ACE2 receptor complex	2.1×10^4	2.1×10^4	fmol mL^{-1}	[31]
$[ANGIV_0]$	angiotensin IV	1	1	fmol mL^{-1}	[29, 45]
$[ANGII \cdot AT1R_0]$	angiotensin II & type 1 receptor complex	85	15	fmol mL^{-1}	[28, 29]
$[ANGII \cdot AT2R_0]$	angiotensin II & type 2 receptor complex	27	5	fmol mL^{-1}	[28, 29]
$[R_0]$	Renin	2.53×10^1	9.43×10^0	fmol mL^{-1}	calculated
β_0	Renin production rate	1.46×10^0	5.45×10^{-1}	fmol mL^{-1} min^{-1}	calculated
k_A	angiotensinogen production rate	1.2×10^3	8.82×10^2	fmol mL^{-1} min^{-1}	calculated
c_A	ANGI to ANGII conversion rate	5.74×10^{-6}	2.34×10^{-6}	#ACE^{-1} min^{-1}	calculated
$k_{ACE2 \cdot ANGII}$	ANGII & ACE2 receptor binding rate	1.47×10^{-6}	3.21×10^{-6}	#ACE2^{-1} min^{-1}	calculated
k_{ACE2}	ANGII–ACE2 to ANG1–7 conversion rate	6.12×10^{-3}	2.39×10^{-3}	min^{-1}	calculated
c_{APA}	ANGII to ANGIV conversion rate	8.89×10^{-3}	4.95×10^{-2}	min^{-1}	calculated
c_{AT1}	ANGII & type 1 receptor binding rate	3.15×10^{-2}	3.09×10^{-2}	min^{-1}	calculated
c_{AT2}	ANGII & type 2 receptor binding rate	1×10^{-2}	1.03×10^{-2}	min^{-1}	calculated
$[MAS \cdot ANG1\text{–}7_0]$	angiotensin 1–7 & MAS receptor complex	1.6×10^1	6.43×10^0	fmol mL^{-1}	calculated

from virtual lung tissue. We further assume $c_{mas} = c_{AT2}$ and solve (S1)–(S11) in the Supplementary File to calculate the patient-specific parameters (Table 2).

2.1.2. COVID-19 immune model

The cell surface ACE2 also acts as a receptor of SARS-CoV-2 entry. In our earlier work, we developed a SARS-CoV-2 tissue simulator [36], which we refer to as the "COVID-19 immune model". Here, we briefly recap the most salient features of the model.

The COVID-19 fibrosis model is developed in an open-source multiscale ABM framework PhysiCell [46] and simulates a tissue section of 800 $\mu m \times$ 800 $\mu m \times$ 20 μm, representing a monolayer of stationary epithelial cells on an alveolar surface of lung tissue. Initially, 2793 epithelial cells, 50 resident macrophages, 28 dendritic cells, and 57 fibroblasts are present in the simulated tissue. We infect the simulated tissue by placing SARS-CoV-2 viral particles in the extracellular space using a uniform random distribution. Viral particles diffuse through tissue and bind with unoccupied or unbound external ACE2 receptors ($ueACE2$) on the epithelial cell surfaces to form bound external ACE2 receptors ($beACE2$). These bound external ACE2 receptors internalize via endocytosis to form bound internal ACE2 receptors ($biACE2$), release the virions to form unbound internal ACE2 receptors ($uiACE2$), and recycle back to the cell surface.

Binding flux (dv_t) between virions and $ueACE2$ depends on the density

of the viral particles near a cell (v_e), volume of the cell (V_c), and binding rate of viral particles to ACE2 receptors (r_b):

$$dv_t = r_b V_c v_e(t) ueACE2(t) \tag{12}$$

where v_e and $ueACE2$ change with time t, through trajectories that emerge from the ABM simulations.

The released virions from $biACE2$ replicate through intracellular viral replication kinetics, export back to the extracellular domain by exocytosis, and diffuse in the tissue. Our model considers the interactions between virion and $ueACE2$ as discrete events, whereas diffusion of the virus in tissue is continuous. Details of the intracellular virus model for replication kinetics, viral response, receptor trafficking, and rules for discrete to continuous transition of the virus are described in much greater detail in our earlier manuscript [36]. Viral infection activates the innate and adaptive immune response and recruits immune cells from the lymph nodes. Further details of the immune and lymph node models are available elsewhere [36, 47].

2.1.3. Fibrosis model

Viral infection and immune response activate latent TGF-β and shift the phenotype of pro-inflammatory M1 macrophages to anti-inflammatory M2 macrophages to produce TGF-β in the later phase of infection, which leads to fibroblast-mediated collagen deposition and fibrosis. Details of the effects of TGF-β sources in fibroblast-mediated collagen deposition at damaged sites of SARS-CoV-2 infected tissue are available in our earlier work [19]. Here, we build upon that work to now consider effects of ACE2 receptor dynamics on fibrosis.

We assume the same initial number and dynamics of ACE and ACE2 receptors. This assumption is based on the experimental observation of similar intensity of ACE and ACE2 protein expressions in lung tissue in the control mice experiments of Roca-Ho et al. [48]. Losses of ACE and ACE2 occur due to epithelial cell death and binding between virus and ACE2 during SARS-CoV-2 infection, which are captured in the COVID-19 immune model of Section 2.1.2. We use the dynamics of $ueACE2$ from the immune model to account for the changes in ACE and ACE2, that is

$$ueACE2(t) = ACE(t) = ACE2(t) \tag{13}$$

The reduction of ACE after infection shifts the homeostasis values of ANGII and downstream RAS peptides downwards. Meanwhile, reduction of

ACE2 acts as double negative feedback for ANGII and increases the systemic concentration of ANGII. With less ACE2 in the lung, ANGII is converted to ACE2•ANG II at a slower rate, providing some surplus of ANGII not converted along this pathway towards ANG1–7. We term the additional ANGII due to loss of ACE2 as "unconverted ANGII". We calculate the unconverted ANGII ($_{ANGII}$) as

$$U_{ANGII}(t) = k_{ACE2\cdot ANGII}[ANGII](ACE2(t_i) - ACE2(t)) \tag{14}$$

where $ACE2(t_i)$ is the number of available ACE2 before time of infection ($t = t_i$), $ACE2(t)$ is the number of available ACE2 at time $t > t_i$ after infection.

We assume that the unconverted ANGII modulates the direct and indirect activation of TGF-β, and we consider first-order reaction kinetics for ANGII-induced TGF-β production rate. Eq. 15 shows the dynamics of TGF-β:

$$\frac{d[T_\beta]}{dt} = k_T U_{ANGII} + k_{MT}[M] + k_{FT}[F] - h_T[T_\beta] \tag{15}$$

where $[T_\beta]$ is TGF-β concentration, k_T is ANGII-induced TGF-β production rate, k_{MT} is TGF-β production rate from macrophages, k_{FT} is TGF-β production rate from fibroblasts, and h_T is degradation rate of TGF-β.

TGF-β-dependent macrophage recruitment rate ($M(T_\beta)$) and fibroblast recruitment rate ($F_g(T_\beta)$) are estimated from the experimental observations of Wahl et al. [41]. Linear interpolation is used for the missing ranges of data. Figure S1 in the Supplementary File shows the dynamics of $M(T_\beta)$ and $F_g(T_\beta)$ with TGF-β. The population balances for macrophages and fibroblasts are

$$\frac{d[M]}{dt} = M(T_\beta) - d_M[M] \tag{16}$$

and

$$\frac{d[F]}{dt} = F_g(T_\beta) - d_F[F] \tag{17}$$

where $[M]$ and $[F]$ are the populations and d_M and d_F are the apoptosis rates of macrophages and fibroblasts, respectively.

The TGF-β-dependent collagen deposition rate from fibroblasts is

$$\frac{d[C]}{dt} = k_{FC}\frac{V_{T\beta}[T_\beta]}{k_{T\beta} + [T_\beta]}[C] \tag{18}$$

where $[C]$ is collagen concentration, k_{FC} is the collagen production rate from fibroblasts, and $V_{T\beta}$ and $k_{T\beta}$ are corresponding rate and saturation parameters defining the TGF-β dependency on collagen deposition [19].

In the fibrosis model, we use the same parameters as our earlier work [19] except parameter values for TGF-β activation rate from a damaged site (DS) and TGF-β secretion rate from an M2 macrophage (MS) are fixed (Table 1), and the initial number of ACE2 receptors per cell is varied ($ueACE2_0$, Table 3) to represent patient groups. The initial values of the immune model variables (Table 3) are all relative to changes from baseline of an uninfected patient rather than absolute numbers and concentrations. The code repository for our earlier fibrosis model is available on github [49], and the underlying COVID-19 lung infection and immune response ABM is also available on github [50].

Table 3: Initial conditions for immune and fibrosis submodels

Symbol	Definition	Initial condition	Unit
$ueACE2_0$	Unoccupied external ACE2 receptors	200-2000	#
$beACE2_0$	Virus-bound external ACE2 receptors	0	#
$biACE2_0$	Virus-bound internal ACE2 receptors	0	#
$ueACE2_0$	Unoccupied internal ACE2 receptors	0	#
$T_{\beta 0}$	Initial concentration of TGF-β	0	ng mL^{-1}
M_0	Initial number of macrophages	0	cells
F_0	Initial number of fibroblasts	0	cells
C_0	Initial amount of collagen	0	μg

2.2. Sensitivity analysis

We use dynamic local sensitivity analysis for parameters and variables to quantify the input parameters and variables that significantly affect the output variables. Eqs. 19–20 show the local sensitivity index for $[ANGII]$ and collagen $[C]$ with respect to the varying one-at-a-time each model parameter (P_i), which is approximated by a difference equation given a small perturbation ΔP_i to the model parameter [33]:

$$\frac{\partial [ANGII]}{\partial P_i} = \lim_{\Delta P_i \to 0^+} \frac{[ANGII](P_i + \Delta P_i, P_{n \neq i}) - [ANGII](P_i, P_{n \neq i})}{\Delta P_i} \quad (19)$$

$$\frac{\partial[C]}{\partial P_i} = \lim_{\Delta P_i \to 0^+} \frac{[C](P_i + \Delta P_i, P_{n \neq i}) - [C](P_i, P_{n \neq i})}{\Delta P_i} \tag{20}$$

where $[ANGII](\mathbf{P})$ and $[C](\mathbf{P})$ are the model predictions evaluated for parameter set $\mathbf{P}$. We normalize the local sensitivity index to eliminate the effect of units. For that, nominal input values (in_s) and output values (out_s) are calculated before varying the parameters. The input values are multiplied by a multiplier (m_S) to change one input at a time. We calculate the change of new input value (in_n) as: $\Delta in(t) = in_n(t) - in_s(t)$ and consider the effect of m_S in input value as: $\Delta in(t) = m_S - 1$. The model for normalized sensitivity index, ($S_{i,t}$), for the predicted new output value (out_n) is shown in Eq. 21.

$$\begin{aligned} S_{i,t} &= \frac{\Delta out(t)}{nominal\ output\ value(t)} \frac{nominal\ input\ value(t)}{\Delta in(t)} \\ &= \frac{out_n(t) - out_s(t)}{out_s(t)} \frac{1}{m_S - 1} \end{aligned} \tag{21}$$

where i denotes parameters or variables, and t denotes time. We applied additional rules to avoid division by zero, as described in Eq. 22.

$$S_{i,t} = \begin{cases} \frac{out_n(t) - out_s(t)}{out_s(t)} \frac{1}{m_S - 1}, & \text{if } out_s(t) > 0 \\ \frac{out_n(t)}{m_S - 1}, & \text{otherwise} \end{cases} \tag{22}$$

2.3. Data extraction

Experimental data used in this paper were extracted from graphs in the original sources, which are referenced in the text, using the open-source Java program Plot Digitizer [51].

3. Results and discussion

The overall model has two phases. In the first phase, we calibrated the RAS model with patient-specific homeostasis peptide concentrations from Table 2 and initial number of ACE2 receptors from the COVID-19 immune model. In the second phase, we first infected the virtual lung tissue for different initial numbers of ACE2 per cell ($ueACE2_0$) using the COVID-19 immune model. Then, we used the predicted $ueACE2$ dynamics from our *in silico* experiments as input for ACE and ACE2 dynamics in the second phase of the overall model where we quantified the effects of patient-group-specific premorbidity (normotensive vs. hypertensive) and ACE2 variations by age and sex in the progression of COVID-19 lung fibrosis.

3.1. In silico experiments to predict COVID-19 lung fibrosis progression with variations of ACE2

3.1.1. Dynamics of ACE2 during SARS-CoV-2 infection

We varied $ueACE2_0$ from 200–2000 with an interval of 200 to account for age and sex differences. The lower ranges of $ueACE2_0$ represent older adults (200-600), intermediate ranges represent middle-aged (800-1200), and upper ranges of $ueACE2_0$ represent young patients (1400-2000). The variations within a range $ueACE2_0$ account for sex differences. We observed increased virion number and persistence with decreasing $ueACE2_0$ (Figure 2). For a higher number of $ueACE2_0$, most of the virions were captured by the nearest cells as the binding flux in Eq. 12 increases with increasing ueACE2. As a result, less virion will be available for diffusion and infecting distant cells from its origin. This process allowed adaptive immunity to become activated and cleared localized virions and infected cells before the spread of infection. The high virion and persistence may relate to the explanations of higher susceptibility and disease severity in older adults due to lower ACE2 expressions.

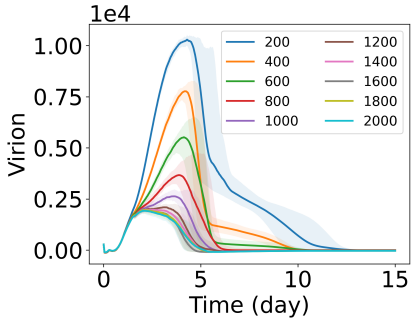

Figure 2: Dynamics of virions for different initial number ACE2 receptors on the cell surface. The lower ranges of ACE2 showed high viral propagation and persistence, representing older adults in our model. The solid lines represent mean and shaded area representing the 5th and 95th percentile of 15 iterations.

Figure 3 shows the dynamics of epithelial cells and ACE2 receptors for 15 days post-infection (dpi). We observed complete destruction of tissue for $ueACE2_0$ 200 and 400, increased cell survivability for ranges between 600–1200, and steady behavior for $ueACE2_0$ of 1400 and above. We did not observe any significant variations in ACE2 dynamics due to viral binding and

internalization of ACE2 ($beACE2$, $biACE2$, and $uiACE2$) as the recycling process moved a portion of internalized ACE2 back to the surface and large availability of surface ACE2 receptors in neighboring uninfected cells. But we observed direct correlation between the dynamics of total number of epithelial cells and ueACE2. We normalized the dynamics of total cells and ueACE2 with their initial value for comparison (Figure 3). The findings suggest that the dysregulation of ACE2 in the lung tissue will mainly occur due loss of major sources of ACE2 by the death of epithelial cells during infection.

3.1.2. Dynamics of immune cells, TGF-β, and collagen

We observed increased latent TGF-β sources (Secreting agent) and M2 macrophages with decreasing $ueACE2_0$ (Figure 4). The increased number of TGF-β sources resulted in higher TGF-β concentrations which effected the activity of fibroblasts and distribution of collagen. We observed localized collagen deposition with lower number of $ueACE2_0$ as lower cell survivability increases the activation of latent TGF-β from extracellular matrix. The increased number of $ueACE2_0$ reduced the activation of latent TGF-β sources, increased cell surviavability, and increased collagen area fractions. In Figure 5, we observed lower collagen area fraction with high amount of collagen deposition for $ueACE2_0$ ranges from 200–800, and higher and steady collagen area fractions with lower amount of collagen deposition for $ueACE2_0$ of 1000 and above. We used the dynamics of ueACE2 in the overall model to account for the changes in ACE2 in the RAS network during disease progression. We compare the total amount of collagen deposition in the virtual lung tissue with additional collagen amount from the patient-group-specific systemic regulation of RAS network in a later section.

3.2. Patient-group-specific local and systemic response before, during, and after infection

Here, we considered four patient groups to account for premorbidity of patients: **group 1** hypertensive patients with no feedback from ANGII•AT1R to renin, **group 2** normotensive patients with no feedback from ANGII•AT1R to renin, **group 3** hypertensive patients with feedback from ANGII•AT1R to renin, and **group 4** normotensive patients with feedback from ANGII•AT1R to renin. Neubauer et al. [52] provided contradictory evidence for direct feedback of ANGII•AT1R to renin in the mice kidney and suggested indirect effects (e.g., blood pressure) as the required concentrations of ANGII to induce renin secretion from renin cells was not achieved in *in vivo* settings.

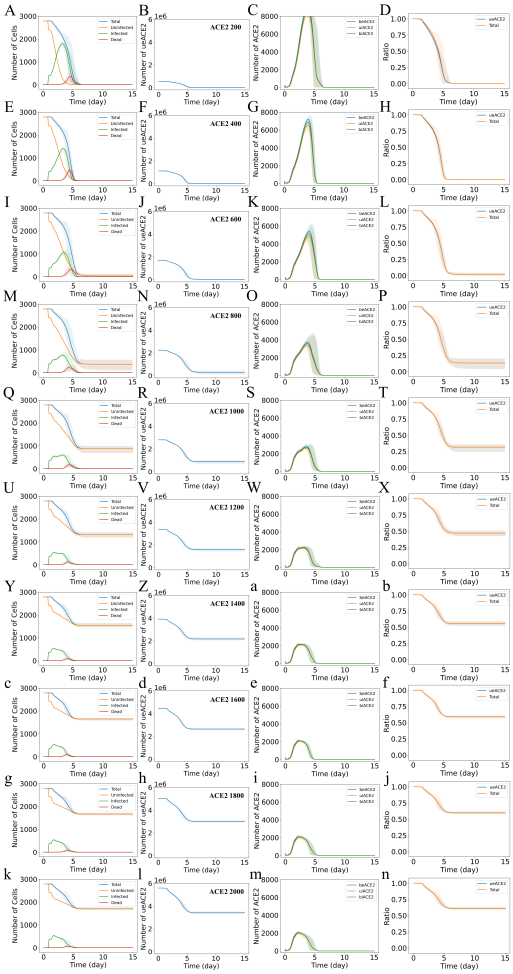

Figure 3: Epithelial cells and ACE2 respond to the different initial values of ACE2. Dynamics of (A, E, I, M, Q, U, Y, c, g, k) total, uninfected, infected, and dead cells, (B, F, J, N, R, V, Z, d, h, l) unbound external ACE2 (ueACE2) (C, G, K, O, S, W, a, e, i, m,) bound external ACE2, bound internal ACE2, unbound internal ACE2, and (D, H, L, P, T, X, b, f, j, n) normalized comparison between the dynamics of ueACE2 and total cells. Each row represents a fixed initial ueACE2 number ranging from 200-2000, top to bottom. The solid lines represent mean and shaded area representing the 5th and 95th percentile of 15 iterations.

But Leete et al. [28] suggested the feedback strength as major difference between male and female RAS. Here, we investigated the response with and

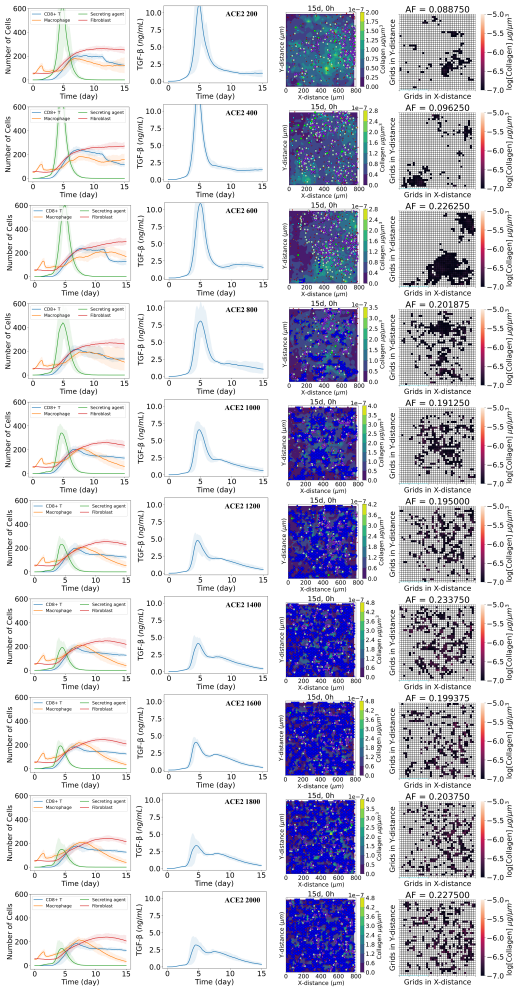

Figure 4: Virtual lung tissue response with variations in the initial number of surface ACE2 receptors and local fibrosis. Column (1) cell population, (2) mean TGF-β concentration, column (3) collagen deposition at damaged sites of tissue at day 15, and column (4) heat map showing collagen area fraction (AF) above the threshold value of 1×10^{-7} μg μm^{-3}. The solid lines represent mean and shaded area represent 5th and 95th percentile of 15 iterations.

without feedback but did not vary the strength of the feedback signaling (δ).

As described in the earlier section, in the first phase, we calibrated the overall model with $ueACE2_0$ from COVID-19 immune model at uninfected condition and ran simulation for 5 days to pre-load patient-group-specific

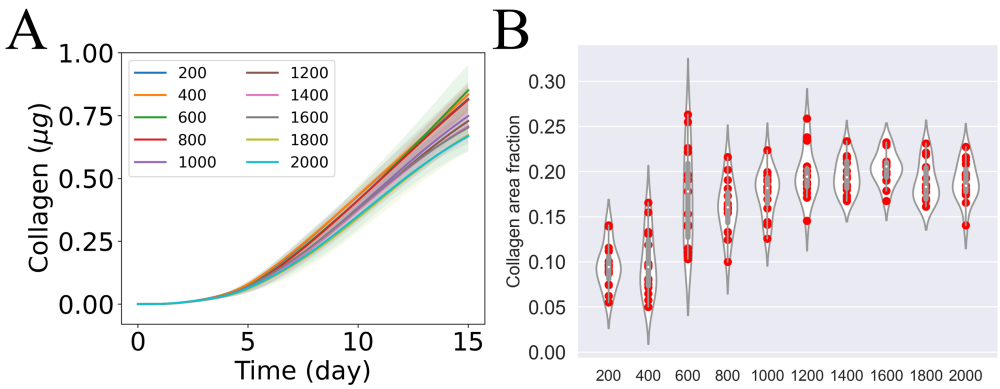

Figure 5: Dynamics of collagen amount and area fraction with variations in initial ACE2. A) collagen amount, solid lines represent mean and shaded area represent 5th and 95th percentile of 15 iterations. and B) collagen area fraction. Violin plots represent distribution, solid red circles represent data for 15 replications in each case, and box plots show median and quartiles.

RAS. The second phase started after 5 days of preloading with the onset of infection where we account for the variations in ACE2 dynamics from COVID-19 immune model. We ran the second phase for 15 dpi and investigated the variations in RAS peptides, immune cells, and fibrosis progression.

3.2.1. Dynamics of RAS peptides with variations in local ACE2 and systemic premorbidity

Figure 6 shows the dynamics of RAS peptides and Figure 7 shows the dose-response of ueACE2 to RAS peptides at 15 dpi. The overall trends in Figure 6–7 illustrate constant renin and AGT, increased ANGI, and decreased ANGII and downstream peptides. We also observed significant variations in the response of RAS peptides for **group 3** and **group 4** for $ueACE2_0$ ranging from 200–600. For these ranges of $ueACE2_0$, ACE2 depleted completely due to the complete destruction of the tissue (Figure 4), which increases the strength of feedback signaling of $ANGII \cdot AT1R$ to renin, resulting in significant increase in the systemic renin.

In Figure 7, we considered the changes in RAS peptides from homeostasis with varying $ueACE2_0$. For $ueACE2_0$ ranges of 200–600, systemic changes in RAS peptides from ANGI and downstream are significant for **group 1**

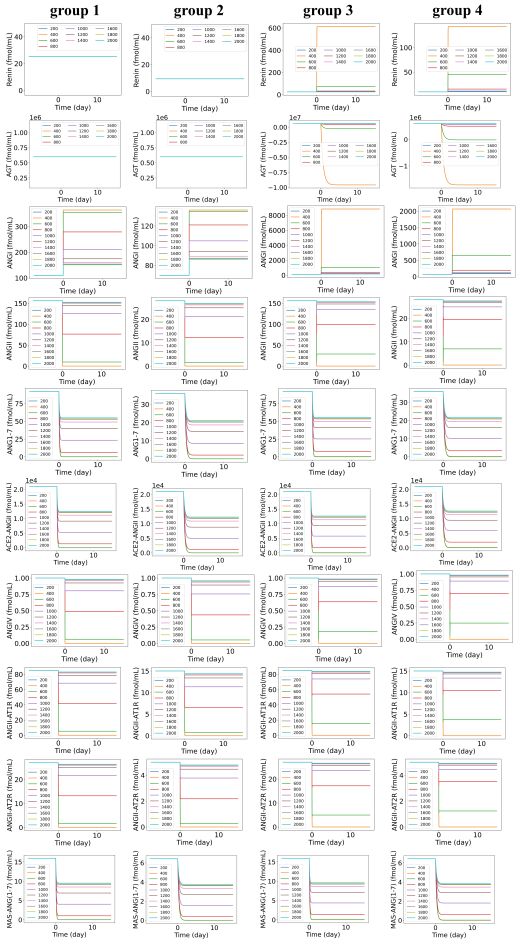

Figure 6: Dynamics of RAS peptides with variation in premorbidity, age, and sex. **group 1:** hypertensive patients with no feedback from ANGII•AT1R to renin, **group 2:** normotensive patients with no feedback from ANGII•AT1R to renin, **group 3:** hypertensive patients with feedback from ANGII•AT1R to renin, and **group 4:** normotensive patients with feedback from ANGII•AT1R to renin.

and **group 2**, and systemic changes in all RAS peptides are significant for **group 3** and **group 4**. We observed the overall trend described earlier for $ueACE2_0$ ranges of 800–1400. **group 3** and **group 4** patients could reduce the changes due to ACE2 variability compared to **group 1** and **group 2** patients using the ANGII•AT1R feedback to renin. We did not observe any significant variations for $ueACE2_0$ of 1600 and above. But response among

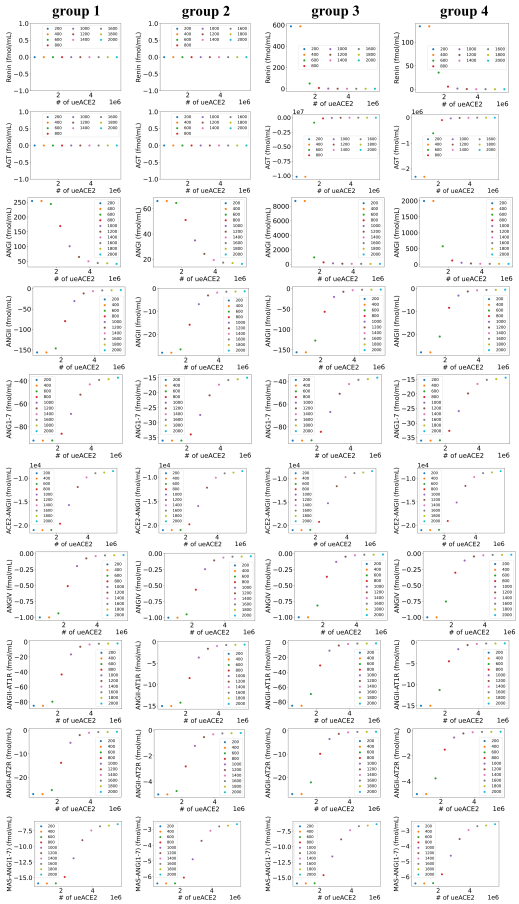

Figure 7: Dose-response of unbound external ACE2 ($ueACE2_0$) to RAS peptides. **group 1:** hypertensive patients with no feedback from ANGII·AT1R to renin, **group 2:** normotensive patients with no feedback from ANGII·AT1R to renin, **group 3:** hypertensive patients with feedback from ANGII·AT1R to renin, and **group 4:** normotensive patients with feedback from ANGII·AT1R to renin.

different groups varies due to premorbidity and feedback signaling.

3.2.2. Model predictions for experimental observed increase and decrease of RAS

Kutz et al. [1] studied patient data to investigate RAS peptide alteration between SARS-CoV-2-positive and SARS-CoV-2-negative patients with respiratory infections. The study design included older adults with premorbid

conditions, such as hypertension, diabetes, and obesity, for both SARS-CoV-2-positive and SARS-CoV-2-negative patients. They observed about 50% lower equilibrium serum RAS peptides and plasma renin activity in SARS-CoV-2-positive patients compared to SARS-CoV-2-negative patients. But no changes were observed in ACE and ACE2 plasma activity.

Our **group 1** patients are most similar to the study of Kutz et al. [1]. In **group 1**, we also observed decreases in RAS peptides with variations of $ueACE2_0$ except for ANGI (Figures 6–7). Figure 8A–B shows the linear fitting of percentage ANGII and ANG1-7 reduction from baseline with variations of $ueACE2_0$ for patient **group 1**. From the linear fitting, we predicted the initial number of $ueACE2_0$, which resulted in the experimentally observed mean decrease of ANGII (52.7% ± 15.8%) and ANG1-7 (64.9% ± 12.9%). We predicted from the linear fitting that 52.7% reduction of ANGII will occur at $ueACE2_0 = 762$ and 64.9% reduction of ANG1-7 will occur at $ueACE2_0 = 1108$ in our model. We hypothesized that the differences in $ueACE2_0$ between ANGII and ANG1-7 for the same cohort arise from the differences in the patient-specific homeostasis RAS peptide concentrations.

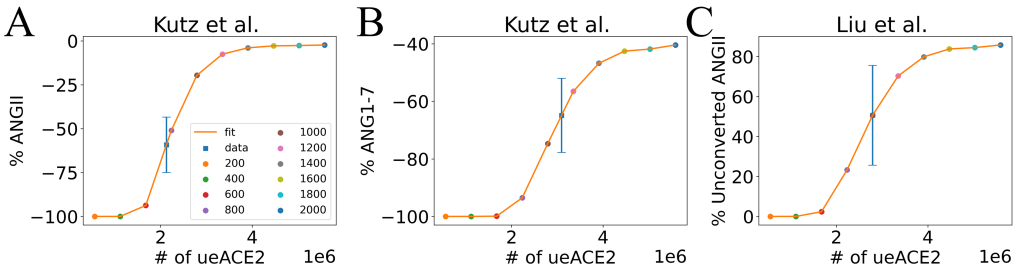

Figure 8: Age and sex correlation with patient data of decreased (Kutz et al.) and increased (Liu et al.) RAS peptides. Prediction of A) ANGII reduction and B) ANG1-7 reduction with the observed decrease in patient data. C) Correlation between unconverted ANGII and increased ANGII in COVID-19 patients.

Contrary to the observations of Kutz et al. [1] we observed increases in ANGI. In our simplified model, we considered constant renin activity to decouple the effect of ACE2 in lung fibrosis. Kutz et al. observed 58.5% reduction in plasma renin activity. We hypothesized that integration of the patient-specific dynamic PRA reduction would account for the experimentally observed reduction in ANGI.

In a separate study, Liu et al. [2] collected plasma samples and demographic data from 55 SARS-CoV-2-positive patients. They reported increased plasma ANGII above the normal range (25-129 pg/mL), mainly in critically ill patients. The measured range of ANGII for the ANGII normal group was 99.4(84.5, 119.1) pg/mL, and ANGII increased group was 149.7(137.8, 165.1) pg/mL. We hypothesized that differences between two SARS-CoV-2 positive groups are due to the reduction of ACE2 by cell death. Unconverted ANGII in our model represents the difference in ANGII between baseline ACE2 ($ACE2(t_i)$) and reduced ACE2 dynamics considering cell death ($ACE2(t > t_i)$. Figure 8C shows the percentage unconverted ANGII increase from baseline with variations of $ueACE2_0$ for patient **group 1**. We predicted the same increase in unconverted ANGII at $ueACE2_0 = 1000$ as the experimental observations of Liu et al. [2]. The predictions also validated parts of our earlier work [19], as $ueACE2_0$ was 1000 in the *in silico* experiments.

3.2.3. Dynamics of fibrosis model with variations in local ACE2 and systemic premorbidity

We considered a simplified first-order reaction kinetics to account for ANGII-induced TGF-β production from unconverted ANGII. The *in vitro* experiments of Lai et al. [53] showed increased TGF-β concentration in human mesangial cells (279-630 pg/mL) with increasing ANGII ranges (0-10^{-7} M). Singh et al. [54] also observed changes in TGF-β concentration from 0.827-1.65 ng/mL with changes of ANGII from the control condition to 10^{-8} M in their in vitro experiments on human mesangial cell. The changes in ANGII in our model occurs at a much slower range compared to these experiments. But similar experiments in lung cells can be used to parameterize k_T. We varied k_T between (1-10)$\times 10^{-4}$ for patient **group 1** and observed linear changes in immune cells and collagen dynamics with variations in k_T (Supplementary file Figure S2).

Figure 9 shows the dynamics of fibrosis model species: U_{ANGII}, TGF-β, immune cells, and collagen, and Figure 10 shows the dose-response of $ueACE2_0$ to imuune model species at 15 dpi. For $ueACE2_0$ ranges of 200–600, the changes in the fibrosis model species are lower compared to ranges 600 and above. We observed the maximum value of fibrosis model species at $ueACE2_0 = 1000$ and a slight reduction after that. The number of macrophages remains constant in response to the changes in $ueACE2_0$ with slight variations in dynamics. The total amount of collagen is higher in **group**

1 and **group 3** patients than in **group 2** and **group 4** patients. We did not observe any significant variations in collagen amount due to ANGII•AT1R feedback to renin. Figure 11 shows the comparison of the total amount of collagen deposition between the overall model and the COVID-19 immune model. We quantified the additional amount of collagen deposition due to the patient group variations by age, sex, and premorbidity. We observed 15%–25% additional amount of collagen deposition depending on the patient group.

However, our observations are subjected to certain limitations. We ran the virtual lung tissue simulator separately and used the predicted data of ueACE2 as input in the RAS model. As a result, we expected overlaps in immune-mediated TGF-β production and contributions to TGF-β from latent TGF-β sources when comparing local and systemic predictions. We also considered a constant renin activity which may change depending on the patient's pre-disease state and progression of disease [1, 28, 31, 33]. We used a constant strength of the feedback signaling to renin (δ), whereas evidence suggested variations in δ depending on sexes [28].

3.3. Sensitivity analysis

The dynamic local sensitivity analysis for parameters and initial values of variables were conducted to quantify the sensitivity of model output collagen and ANGII with input parameters. The analyses were performed for the parameters: β, k_A, c_A, c_R, $k_{ACE2 \cdot ANGII}$, k_{ACE2}, c_{APA}, c_{AT1}, c_{AT2}, k_{MT}, k_{FT}, k_{FC}, and variables: $[R_0]$, $[AGT_0]$, $[ANGI_0]$, $[ANGII_0]$, $[ANG1\text{–}7_0]$, $[ACE2 \cdot ANGII_0]$, $[ANGIV_0]$, $[ANGII \cdot AT1R_0]$, $[ANGII \cdot AT2R_0]$, $[MAS \cdot ANG1\text{–}7_0]$. We ran the sensitivity analyses using $m_S = [0.1, 0.3, 0.5, 0.7, 0.9, 1.1, 1.5, 2, 5, 10]$ as input. Figure 12 and 13 shows the dynamic local sensitivity for parameters and variables, respectively for **group 1** patients. In Figure 12, we observed parameters k_A, β, $k_{ACE2 \cdot ANGII}$, c_A, and k_{MT} and sensitive to collagen response in descending order with no sensitivity to parameters before infection. The sensitivity analysis of ANGII shows parameters β, c_A, and $k_{ACE2 \cdot ANGII}$ will change the steady state of ANGII before infection. Parameters c_A, and $k_{ACE2 \cdot ANGII}$ modulate ANGII response positively and negatively, respectively, before infection and positively after infection. In Figure 13, we observed initial values of variables: $[ANGII_0]$, $[ANG1\text{–}7_0]$, and $[ANGI_0]$ are sensitive variables for collagen response which varies significantly depending on m_S. The sensitivity analysis

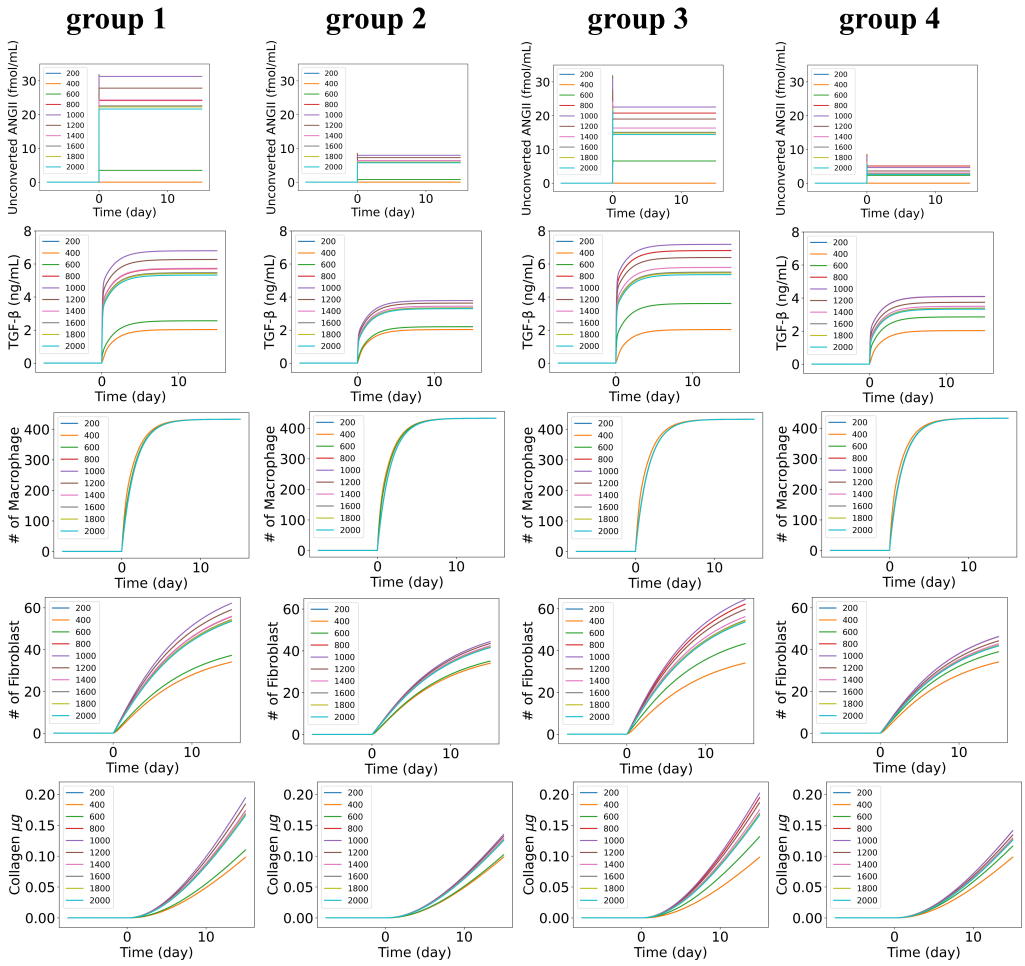

Figure 9: The dynamics of TGF-β, immune cells, and collagen vary in premorbidity, age, and sex. **group 1:** hypertensive patients with no feedback from ANGII·AT1R to renin, **group 2:** normotensive patients with no feedback from ANGII·AT1R to renin, **group 3:** hypertensive patients with feedback from ANGII·AT1R to renin, and **group 4:** normotensive patients with feedback from ANGII·AT1R to renin.

of ANGII shows initial values of variables $[ANGI_0]$ and $[ANG1\text{–}7_0]$ effect ANGII response negatively and positively, respectively.

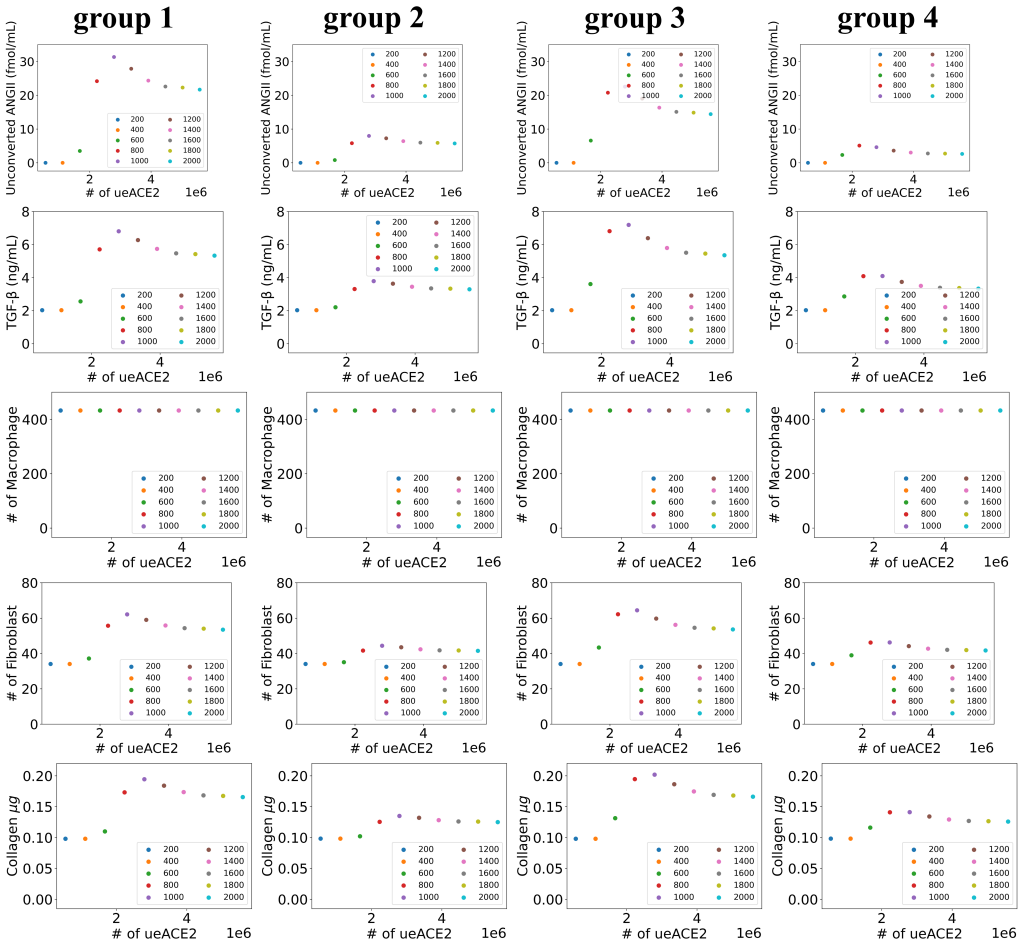

Figure 10: Dose-response of unbound external ACE2 to TGF-β, immune cells, and collagen. **group 1:** hypertensive patients with no feedback from $ANGII \cdot AT1R$ to renin, **group 2:** normotensive patients with no feedback from $ANGII \cdot AT1R$ to renin, **group 3:** hypertensive patients with feedback from $ANGII \cdot AT1R$ to renin, and **group 4:** normotensive patients with feedback from $ANGII \cdot AT1R$ to renin.

4. Conclusion

Heterogeneity in the severity of COVID-19 disease depends on the patient-specific premorbid condition, age, and sex differences. We developed an integrated mathematical model to investigate and quantify the effect of these heterogeneous factors in COVID-19 lung fibrosis. We observed increases in

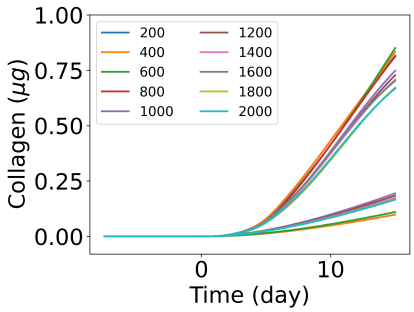

Figure 11: Local and systemic contribution of collagen in the lung. The steeper slope group represents local contributions, whereas the flatter slope group represents systemic contribution due to premorbidity, age, and sex in RAS.

the number and persistence of virus and disease severity at lower cell surface ACE2 receptors. We identified cell death as major reduction source of ACE2 and did not observe any significant difference due to viral-bound ACE2. Our results predicted the mechanisms for conflicting RAS alterations in two previous experimental studies. We also quantified the local and systemic contribution of collagen from immune dysregulation and RAS alteration in COVID-19 lung fibrosis. Our model may find application in the calibrations of patent-specific local and systemic regulations of RAS with bleomycin-induced tissue fibrosis model and autopsy and biopsy tissue samples of patients.

Supporting information

Supplementary File. The Supplementary File contains supporting information and figures organized into the following sections: steady state solution of RAS; TGF-β-dependent macrophage and fibroblast recruitment; effects of variations in k_T on TGF-β, immune cells, and collagen deposition.

Acknowledgment

This work was supported by the National Institutes of Health grant R35GM133763 and the University at Buffalo, and the Center for Computational Research at the University at Buffalo [55]. We thank the scientific community for model feedback, including Paul Macklin, Michael Getz, Amber M. Smith, Thomas Hillen, and Yafei Wang.

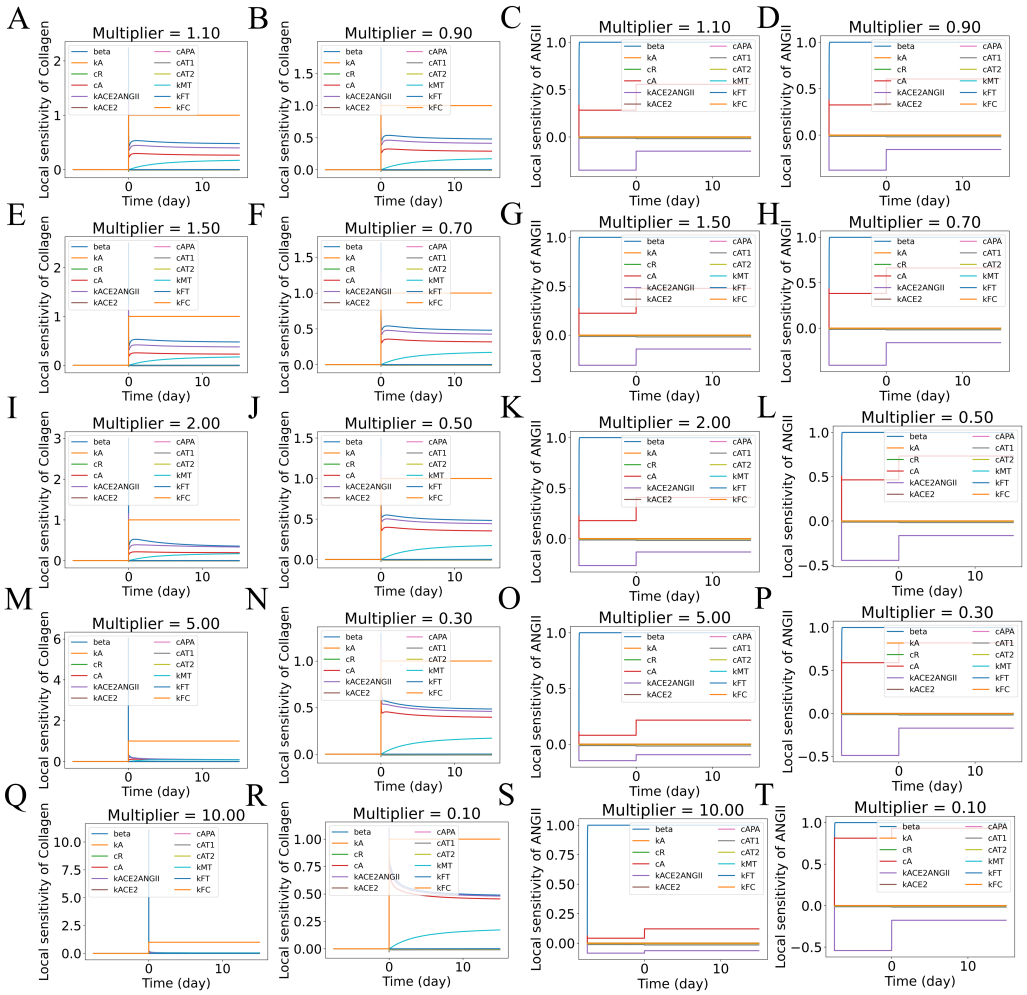

Figure 12: Local sensitivity analysis of parameters for ANGII and collagen for pateint **group 1:** hypertensive patients with no feedback from ANGII·AT1R to renin.

References

[1] A. Kutz, A. Conen, C. Gregoriano, S. Haubitz, D. Koch, O. Domenig, L. Bernasconi, B. Mueller, P. Schuetz, Renin-angiotensin-aldosterone system peptide profiles in patients with COVID-19, European Journal of Endocrinology 184 (2021) 543–552.

[2] N. Liu, Y. Hong, R. G. Chen, H. M. Zhu, High rate of increased level

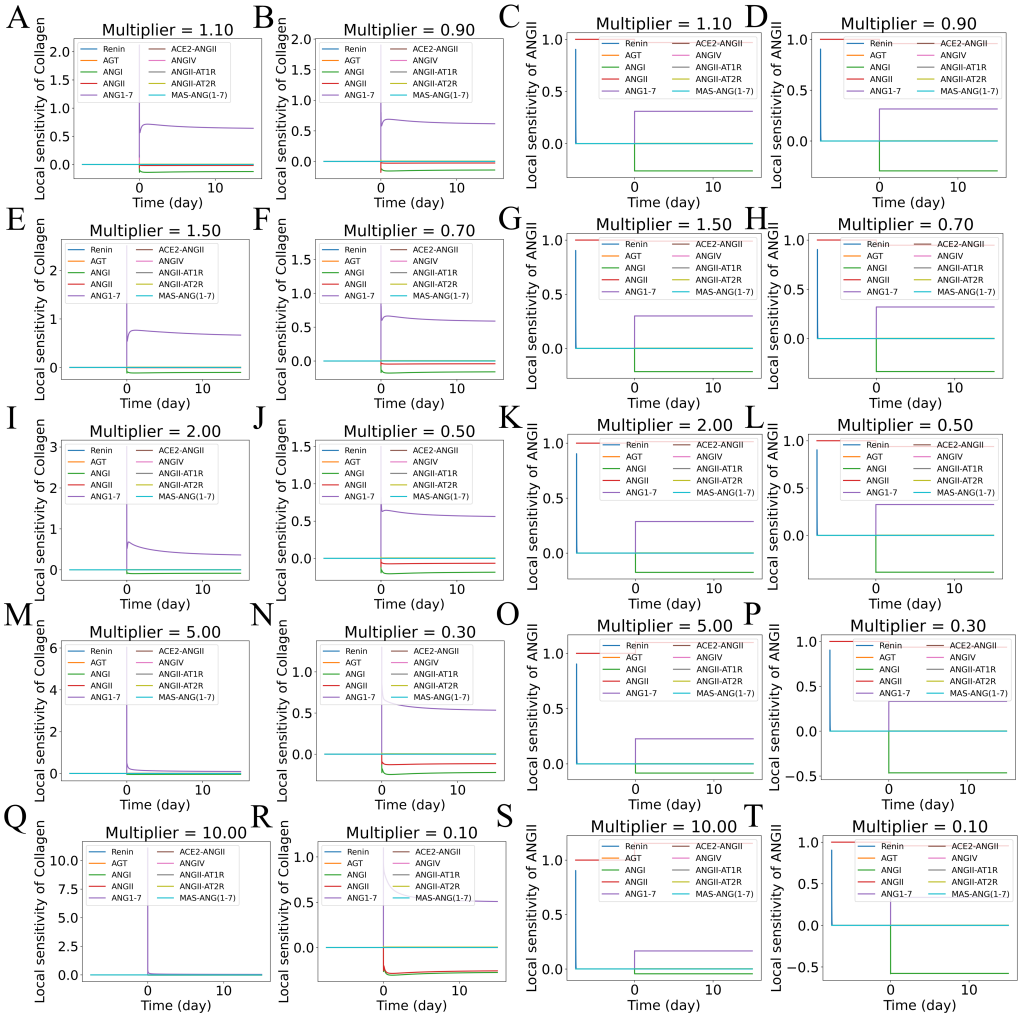

Figure 13: Local sensitivity analysis of initial values of variables for ANGII and collagen for pateint **group 1:** hypertensive patients with no feedback from ANGII•AT1R to renin.

of plasma angiotensin II and its gender difference in COVID-19: an analysis of 55 hospitalized patients with COVID-19 in a single hospital, WuHan, China, medRxiv (2020).

[3] F. L. Martins, C. A. Tavares, P. A. Malagrino, T. Rentz, A. Benetti, T. M. Rios, G. M. Pereira, B. Caramelli, S. K. Teixeira, J. E. Krieger,

et al., Sex differences in the lung ACE/ACE2 balance in hypertensive rats, Bioscience Reports 41 (2021) BSR20211201.

[4] P. Pagliaro, C. Penna, ACE/ACE2 ratio: a key also in 2019 coronavirus disease (Covid-19)?, Frontiers in Medicine 7 (2020) 335.

[5] L. M. Hilliard, A. K. Sampson, R. D. Brown, K. M. Denton, The "his and hers" of the renin-angiotensin system, Current Hypertension Reports 15 (2013) 71–79.

[6] Y. Liu, Y. Yang, C. Zhang, F. Huang, F. Wang, J. Yuan, Z. Wang, J. Li, J. Li, C. Feng, et al., Clinical and biochemical indexes from 2019-nCoV infected patients linked to viral loads and lung injury, Science China Life Sciences 63 (2020) 364–374.

[7] H. Zhang, W. Shang, Q. Liu, X. Zhang, M. Zheng, M. Yue, Clinical characteristics of 194 cases of COVID-19 in Huanggang and Taian, China, Infection 48 (2020) 687–694.

[8] U. Kintscher, A. Slagman, O. Domenig, R. Röhle, F. Konietschke, M. Poglitsch, M. Möckel, Plasma angiotensin peptide profiling and ACE (angiotensin-converting enzyme)-2 activity in COVID-19 patients treated with pharmacological blockers of the renin-angiotensin system, Hypertension 76 (2020) e34–e36.

[9] K. D. Pendergrass, N. T. Pirro, B. M. Westwood, C. M. Ferrario, K. B. Brosnihan, M. C. Chappell, Sex differences in circulating and renal angiotensins of hypertensive mRen. lewis but not normotensive Lewis rats, American Journal of Physiology-Heart and Circulatory Physiology 295 (2008) H10–H20.

[10] X. Xudong, C. Junzhu, W. Xingxiang, Z. Furong, L. Yanrong, Age-and gender-related difference of ACE2 expression in rat lung, Life Sciences 78 (2006) 2166–2171.

[11] U. Bastolla, Mathematical model of SARS-Cov-2 propagation versus ACE2 fits COVID-19 lethality across age and sex and predicts that of SARS, Frontiers in Molecular Biosciences 8 (2021) 676.

[12] W. Miesbach, Pathological role of angiotensin II in severe COVID-19, TH Open 4 (2020) e138–e144.

[13] J. Yim, H. H. Lim, Y. Kwon, COVID-19 and pulmonary fibrosis: therapeutics in clinical trials, repurposing, and potential development, Archives of Pharmacal Research 44 (2021) 499–513.

[14] J. Wigén, A. Löfdahl, L. Bjermer, L. E. Rendin, G. Westergren-Thorsson, Converging pathways in pulmonary fibrosis and Covid-19-the fibrotic link to disease severity, Respiratory Medicine X 2 (2020) 100023.

[15] A. M. Murphy, A. L. Wong, M. Bezuhly, Modulation of angiotensin II signaling in the prevention of fibrosis, Fibrogenesis & Tissue Repair 8 (2015) 1–7.

[16] R. P. Marshall, P. Gohlke, R. C. Chambers, D. C. Howell, S. E. Bottoms, T. Unger, R. J. McAnulty, G. J. Laurent, Angiotensin II and the fibroproliferative response to acute lung injury, American Journal of Physiology-Lung Cellular and Molecular Physiology 286 (2004) L156–L164.

[17] G. H. Gibbons, R. Pratt, V. J. Dzau, et al., Vascular smooth muscle cell hypertrophy vs. hyperplasia. Autocrine transforming growth factor-beta 1 expression determines growth response to angiotensin II, The Journal of Clinical Investigation 90 (1992) 456–461.

[18] S. Kagami, W. A. Border, D. E. Miller, N. A. Noble, et al., Angiotensin II stimulates extracellular matrix protein synthesis through induction of transforming growth factor-beta expression in rat glomerular mesangial cells, The Journal of Clinical Investigation 93 (1994) 2431–2437.

[19] M. A. Islam, M. Getz, P. Macklin, A. N. Ford Versypt, An agent-based modeling approach for lung fibrosis in response to COVID-19, bioRxiv (2022).

[20] M. Ceresa, A. L. Olivares, J. Noailly, M. A. González Ballester, Coupled immunological and biomechanical model of emphysema progression, Frontiers in Physiology 9 (2018) 388.

[21] Y. F. Jin, H. C. Han, J. Berger, Q. Dai, M. L. Lindsey, Combining experimental and mathematical modeling to reveal mechanisms of macrophage-dependent left ventricular remodeling, BMC Systems Biology 5 (2011) 1–14.

[22] L. Mecozzi, M. Mambrini, F. Ruscitti, E. Ferrini, R. Ciccimarra, F. Ravanetti, N. Sverzellati, M. Silva, L. Ruffini, S. Belenkov, et al., In-vivo lung fibrosis staging in a bleomycin-mouse model: a new micro-CT guided densitometric approach, Scientific Reports 10 (2020) 1–12.

[23] X. Li, M. Molina-Molina, A. Abdul-Hafez, V. Uhal, A. Xaubet, B. D. Uhal, Angiotensin converting enzyme-2 is protective but downregulated in human and experimental lung fibrosis, American Journal of Physiology-Lung Cellular and Molecular Physiology 295 (2008) L178–L185.

[24] G. Rey-Parra, A. Vadivel, L. Coltan, A. Hall, F. Eaton, M. Schuster, H. Loibner, J. Penninger, Z. Kassiri, G. Oudit, et al., Angiotensin converting enzyme 2 abrogates bleomycin-induced lung injury, Journal of Molecular Medicine 90 (2012) 637–647.

[25] K. Kuba, Y. Imai, S. Rao, H. Gao, F. Guo, B. Guan, Y. Huan, P. Yang, Y. Zhang, W. Deng, et al., A crucial role of angiotensin converting enzyme 2 (ACE2) in SARS coronavirus-induced lung injury, Nature medicine 11 (2005) 875–879.

[26] Y. Imai, K. Kuba, S. Rao, Y. Huan, F. Guo, B. Guan, P. Yang, R. Sarao, T. Wada, H. Leong-Poi, et al., Angiotensin-converting enzyme 2 protects from severe acute lung failure, Nature 436 (2005) 112–116.

[27] L. Wang, Y. Wang, T. Yang, Y. Guo, T. Sun, Angiotensin-converting enzyme 2 attenuates bleomycin-induced lung fibrosis in mice, Cellular Physiology and Biochemistry 36 (2015) 697–711.

[28] J. Leete, S. Gurley, A. T. Layton, Modeling sex differences in the renin angiotensin system and the efficacy of antihypertensive therapies, Computers & Chemical Engineering 112 (2018) 253–264.

[29] F. Pucci, P. Bogaerts, M. Rooman, Modeling the molecular impact of SARS-CoV-2 infection on the renin-angiotensin system, Viruses 12 (2020) 1367.

[30] M. Sadria, A. T. Layton, Use of angiotensin-converting enzyme inhibitors and angiotensin II receptor blockers during the COVID-19 pandemic: a modeling analysis, PLoS Computational Biology 16 (2020) e1008235.

[31] C. Voutouri, M. R. Nikmaneshi, C. C. Hardin, A. B. Patel, A. Verma, M. J. Khandekar, S. Dutta, T. Stylianopoulos, L. L. Munn, R. K. Jain, In silico dynamics of COVID-19 phenotypes for optimizing clinical management, Proceedings of the National Academy of Sciences 118 (2021) e2021642118.

[32] P. Barbiero, P. Lió, The computational patient has diabetes and a COVID, arXiv preprint arXiv:2006.06435 (2020).

[33] A. N. Ford Versypt, G. K. Harrell, A. N. McPeak, A pharmacokinetic/pharmacodynamic model of ace inhibition of the renin-angiotensin system for normal and impaired renal function, Computers & Chemical Engineering 104 (2017) 311–322.

[34] M. R. Pilvankar, M. A. Higgins, A. N. Ford Versypt, Mathematical model for glucose dependence of the local renin-angiotensin system in podocytes, Bulletin of Mathematical Biology 80 (2018) 880–905.

[35] M. R. Pilvankar, H. L. Yong, A. N. Ford Versypt, A glucose-dependent pharmacokinetic/pharmacodynamic model of ace inhibition in kidney cells, Processes 7 (2019) 131.

[36] M. Getz, Y. Wang, G. An, A. Becker, C. Cockrell, N. Collier, M. Craig, C. L. Davis, J. Faeder, A. N. Ford Versypt, T. Mapder, J. F. Gianlupi1, J. A. Glazier, S. Hamis, R. Heiland, T. Hillen, D. Hou, M. A. Islam, et al., Iterative community-driven development of a SARS-CoV-2 tissue simulator, BioRxiv (2021).

[37] K. M. Hallow, A. Lo, J. Beh, M. Rodrigo, S. Ermakov, S. Friedman, H. de Leon, A. Sarkar, Y. Xiong, R. Sarangapani, et al., A model-based approach to investigating the pathophysiological mechanisms of hypertension and response to antihypertensive therapies: extending the Guyton model, American Journal of Physiology-Regulatory, Integrative and Comparative Physiology 306 (2014) R647–R662.

[38] W. Hao, C. Marsh, A. Friedman, A mathematical model of idiopathic pulmonary fibrosis, PLoS One 10 (2015) e0135097.

[39] A. B. Roberts, M. B. Sporn, R. K. Assoian, J. M. Smith, N. S. Roche, L. M. Wakefield, U. I. Heine, L. A. Liotta, V. Falanga, J. H. Kehrl,

Transforming growth factor type beta: rapid induction of fibrosis and angiogenesis in vivo and stimulation of collagen formation in vitro, Proceedings of the National Academy of Sciences 83 (1986) 4167–4171.

[40] R. A. Ignotz, J. Massague, Transforming growth factor-beta stimulates the expression of fibronectin and collagen and their incorporation into the extracellular matrix, Journal of Biological Chemistry 261 (1986) 4337–4345.

[41] S. M. Wahl, D. A. Hunt, L. M. Wakefield, N. McCartney-Francis, L. M. Wahl, A. B. Roberts, M. B. Sporn, Transforming growth factor type beta induces monocyte chemotaxis and growth factor production, Proceedings of the National Academy of Sciences 84 (1987) 5788–5792.

[42] A. Katsurada, Y. Hagiwara, K. Miyashita, R. Satou, K. Miyata, N. Ohashi, L. G. Navar, H. Kobori, Novel sandwich ELISA for human angiotensinogen, American Journal of Physiology-Renal Physiology 293 (2007) F956–F960.

[43] M. C. Chappell, Biochemical evaluation of the renin-angiotensin system: the good, bad, and absolute?, American Journal of Physiology-Heart and Circulatory Physiology 310 (2016) H137–H152.

[44] J. C. Sullivan, P. Rodriguez-Miguelez, M. A. Zimmerman, R. A. Harris, Differences in angiotensin (1-7) between men and women, American Journal of Physiology-Heart and Circulatory Physiology 308 (2015) H1171–H1176.

[45] J. Nussberger, D. B. Brunner, B. Waeber, H. R. Brunner, Specific measurement of angiotensin metabolites and in vitro generated angiotensin II in plasma., Hypertension 8 (1986) 476–482.

[46] A. Ghaffarizadeh, R. Heiland, S. H. Friedman, S. M. Mumenthaler, P. Macklin, Physicell: An open source physics-based cell simulator for 3-D multicellular systems, PLoS Computational Biology 14 (2018) e1005991.

[47] A. L. Jenner, R. A. Aogo, S. Alfonso, V. Crowe, X. Deng, A. P. Smith, P. A. Morel, C. L. Davis, A. M. Smith, M. Craig, COVID-19 virtual patient cohort suggests immune mechanisms driving disease outcomes, PLoS Pathogens 17 (2021) e1009753.

[48] H. Roca-Ho, M. Riera, V. Palau, J. Pascual, M. J. Soler, Characterization of ACE and ACE2 expression within different organs of the NOD mouse, International Journal of Molecular Sciences 18 (2017) 563.

[49] M. A. Islam, A. N. Ford Versypt, covid19fibrosis, 2022. DOI: 10.5281/zenodo.7295144. http://github.com/ashleefv/covid19fibrosis (accessed 11.05.22).

[50] R. Heiland, P. Macklin, pc4covid19, 2022. DOI: 10.5281/zenodo.5644308. http://github.com/pc4covid19/pc4covid19/releases/tag/v5.0 (accessed 11.05.22).

[51] SourceForge, Plot Digitizer (2015). (Online; accessed 21-October-2021), `http://plotdigitizer.sourceforge.net/`.

[52] B. Neubauer, J. Schrankl, D. Steppan, K. Neubauer, M. L. Sequeira-Lopez, L. Pan, R. A. Gomez, T. M. Coffman, K. W. Gross, A. Kurtz, et al., Angiotensin II short-loop feedback: is there a role of Ang II for the regulation of the renin system in vivo?, Hypertension 71 (2018) 1075–1082.

[53] K. N. Lai, S. C. Tang, J.-Y. Guh, T.-D. Chuang, M. F. Lam, L. Y. Chan, A. W. Tsang, J. C. Leung, Polymeric IgA1 from patients with IgA nephropathy upregulates transforming growth factor-β synthesis and signal transduction in human mesangial cells via the renin-angiotensin system, Journal of the American Society of Nephrology 14 (2003) 3127–3137.

[54] R. Singh, N. Alavi, A. K. Singh, D. J. Leehey, Role of angiotensin II in glucose-induced inhibition of mesangial matrix degradation, Diabetes 48 (1999) 2066–2073.

[55] Center for Computational Research, University at Buffalo (2019). (Online; accessed 14-April-2022), `http://hdl.handle.net/10477/79221`.